# Data acquisition, processing and filtering for reliable 3D resistivity and time-domain induced polarisation tomography in an urban area
## Field example of Vinsta, Stockholm

Rossi, Matteo; Dahlin, Torleif; Olsson, Per Ivar; Günther, Thomas

# Data acquisition, processing and filtering for reliable 3D resistivity and time-domain induced polarisation tomography in an urban area: field example of Vinsta, Stockholm

Matteo Rossi[1*], Torleif Dahlin[1], Per-Ivar Olsson[1] and Thomas Günther[2]

[1] *Engineering Geology, Lund University, Lund, Sweden*

[2] *Leibniz Institute for Applied Geophysics (LIAG), Hannover, Germany*

### ABSTRACT

There is an increasing demand for trustworthy engineering geological conceptual models in urban areas due to an increasing trend in the underground infrastructure construction. Good-quality site investigations can reduce the risk of encountering unexpected geological conditions during construction. Geoelectrical measurements can be used as a tool for providing an overview of the site conditions and serve as a base for planning a geotechnical drilling program and for integration of the results. Geophysical surveys in urban environments may encounter problems due to strict logistical constraints and may be severely affected by electric and electromagnetic noise. Careful processing of the data is necessary to obtain a reliable estimation of the electrical properties of the ground, both electrical resistivity and chargeability.

A large three-dimensional dataset was acquired in the suburban area of Stockholm (Sweden), with the aim of investigating a weak zone in the crystalline bedrock, which had been pointed out by prior geological and geotechnical surveys. Full waveforms of potential dipoles were recorded and processed for removing harmonic noise and background drift. Moreover, a statistical algorithm for handling the quality of the full-waveform shapes has been proposed. The goodness-of-fit test identifies full waveforms with noise that derives from direct current injections, caused by grounding spots of the adjacent metro line.

The processed dataset is inverted for electrical resistivity and integral chargeability. The results image a large three-dimensional volume of the underground. The inverted distribution of geophysical quantities marks out the presence of a wide zone of weak rock, which was not identified by geotechnical probing in the site investigation but documented during the construction phase. Such zones can potentially cause severe problems during the construction of underground infrastructure.

**Key words:** 3D resistivity inversion, Induced polarization, Signal processing

## INTRODUCTION

The growing urbanisation in many regions around the world reduces the availability of space for new infrastructures; hence, there is a trend towards going underground with the constructions in cities, i.e., underground railways, roads, tunnels, and communication facilities. Geology is the most important factor for the design, construction, and the cost of underground constructions, and unexpected geological conditions generally cause the most severe delays and extra cost (e.g., Bell 2006). In order to avoid costly changes in the building process due to unexpected site conditions, good-quality information about the underground is required. This demands sufficient and relevant pre-investigations of good quality.

Geotechnical drilling traditionally dominates the site investigations, but it provides only local information, even though it is essential for design. Geophysical methods can produce large and laterally continuous 2D/3D images of the subsurface properties at reasonable cost, but they are limited by resolution and ambiguities in the interpretation. The combination of geotechnical probing and geophysical imaging can lead to a comprehensive overview of the underground structures, the distribution of lithologies, and the properties of materials (Cavinato *et al.* 2006; Danielsen and Dahlin 2009; Rønning *et al.* 2014). The building of a reliable engineering-geological conceptual model can

---

* matteo.rossi@tg.lth.se
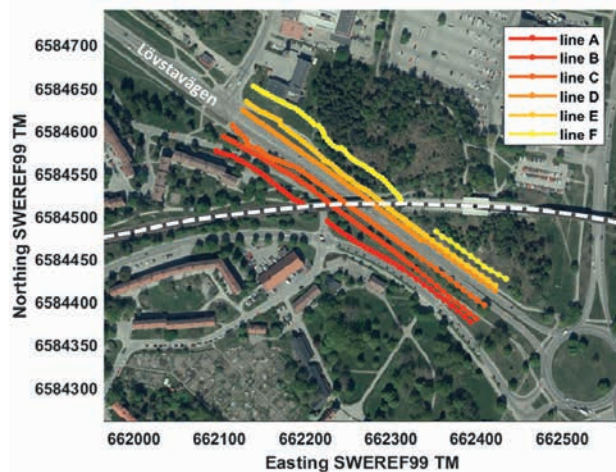
**Figure 1** Orthophoto of the study area with the main road (Lövstavägen) and the railway tracks. The coloured lines (from red to yellow) show the DCIP layout. The white dashed line highlights the presence of the metro train tracks (original orthophoto from Lantmäteriet, 2016). Coordinate system Sweref 99 TM.
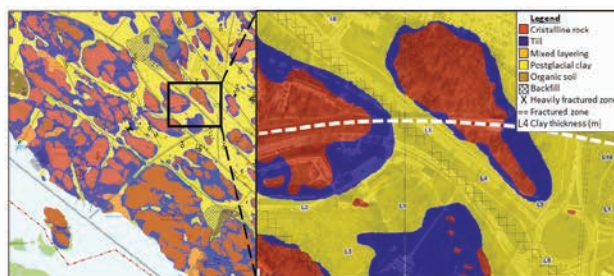


**Figure 2** On the left, the general geology map of the area. On the right, a zoomed-in picture of the geological setting on top of the orthophoto. The white dashed line highlights the presence of the metro tracks (original geological map and ortophoto from Geoarkivet, 2017).

reduce the risk of encountering unexpected geological conditions, and consequently minimise delays and extra costs in the construction works. Moreover, geophysical methods can provide information about ground stability, archaeological settings, and groundwater vulnerability.

An example of an extensive geophysical survey in an urban environment via refraction seismic can be found in Malehmir *et al.* (2015). Electrical resistivity tomography (ERT) is a well-established technique for site investigation, and it has been applied for the characterisation of sites in urban locations. Cardarelli *et al.* (2010) applied seismic refraction and ERT for looking at cavities in the city of Rome. ERT can provide useful information about ground deformation and slope stability in connection with inhabited areas (Perrone *et al.* 2006; Perrone *et al.* 2008). Archeological pre-investigations in cities can be carried out through ERT techniques (Tsokas *et al.* 2008; Papadopoulos *et al.* 2009). The characterisation of rock masses, aiming for discontinuities and weak zones, in support of underground con-

structions (i.e., tunnelling) can be accomplished also via geoelectrical measurements (Ganerød *et al.* 2006; Danielsen and Dahlin 2009; Bellmunt *et al.* 2012; Rønning *et al.* 2014).

Geophysical measurements in urban areas are challenging, due to various noise sources and spatial restrictions caused by infrastructures. In particular, large geoelectrical surveys may be severely affected by environmental noise, both electrical and electromagnetic (Olsson *et al.* 2016).

In the present work, a large 3D acquisition of direct-current (DC) resistivity and time-domain induced polarisation (DCIP) was performed to investigate the suburban environment of Stockholm (Sweden), where an underground infrastructure is planned. A detailed description of the engineering geology for underground construction around Stockholm is reported by Morfeldt (1993). The aim is the mapping of a possible geotechnical weak zone in the bedrock, where the construction will take place. The recording of potential full waveforms leads to an accurate post-processing of the dataset, improving the quality and reducing the uncertainties of the data.

## SITE DESCRIPTION

The present work is an example of a DCIP survey, carried out in an urban environment. The investigated area is located in the municipality of Vinsta, about 10 km WNW of Stockholm (Sweden). An underground infrastructure was planned in the area, more precisely in the northwestern part of the DCIP layout, north of the metro line bridge (Figure 1). The designed construction is an access ramp to a motorway tunnel, which will be located in the shallower underground (max. 20 m deep). The dual road tunnels and their access ramps are part of the E4 Stockholm Bypass Project (Förbifart Stockholm).

The main goal of the geophysical survey was to map a weak zone in the bedrock, through which the tunnel will be constructed. The poor-quality rock is located along an existing four-lane road, Lövstavägen, where geotechnical *in situ* measurements have been made prior to this survey.

The landscape is generated by the glacial activity of the last land ice cap, retreating across Sweden from 20,000 years ago. The glacial erosion created a hummocky land: knolls of massive rock separated by hollows and depressions filled with quaternary sedimentary deposits.

The geological setting is summarised in Figure 2. Crystalline basement outcrops are mainly located on topographically elevated areas, and they comprise pre-Cambrian rocks that belong to the Svecofennian Orogeny (Stålhös 1968, 1969). In the Stockholm region, the bedrock consists of acidic intrusive rocks from granite to granodiorite. In the bedrock depressions between the outcrops, the rock mass is covered by a layer of till, few metres thick. On top of the glacial deposit rests a layer of lacustrine post-glacial clay and silty clay. From the geological map, it is clear that the bedrock depressions are located in conjunction with tectonic lineaments, which acted as preferential zones for glacial erosion. According to Figure 2, a large interpreted frac-

ture zone is likely to affect the crystalline rock mass along the four-lane road that crosses in the middle of our DCIP layout.

## METHODOLOGY

A 3D DCIP survey was performed from the 20th to the 22nd of October, 2015. The layout consisted of six lines, approximately parallel to the main road (Figure 1), i.e., three lines on the southern side and three lines on the northern side, covering an area of approximately 350 m × 75 m, elongated in a NW–SE direction. The lines were labelled from A to F, from the most southern position to the northern one, respectively. Each line had 64 electrodes, with the exception of Lines A and F, which had a gap due to practical issues related to urban infrastructure, as it is clearly visible in Figure 1 (railway bridge and roads). The total number of electrodes was 357. The electrode spacing along the lines was variable: 5 m for the first 54 electrodes in the northwestern portion of the line; 10 m in the remaining southeastern part. The larger electrode spacing in the southeastern part of the investigated area was due to the intention of increasing the length of the profiles to obtain deeper information, as we were outside the area of interest and we were not aiming for a good resolution in the shallower part. Standard acid-grade stainless steel electrode rods were placed in the ground where it was possible (i.e., on greenswards and soil), avoiding roads. Where the terrain is characterised by outcrops (e.g., Line F), acid-grade stainless steel electrode plates (a square 20 cm × 20 cm) were put in contact with the rock using a conductive gel. The contact resistances were generally below 5 KΩ and, in a few cases, between 5 KΩ and 10 KΩ. A couple of electrodes that showed higher contact resistance were removed from the datasets.

We acquired several datasets with different electrode configurations: six 2D gradient arrays, one along each line, and six different cross-line arrays (including equatorial dipole–dipole, equatorial gradient, orthogonal, and diagonal; see Loke *et al.* 2014) with different quadrupole lengths, resulting in a total of 15,539 measurements. The characteristics of the acquired arrays are summarised in Table 1.

The 2D arrays along the parallel lines had multiple-gradient configurations (Dahlin and Zhou 2005), where different lines have were measured and different parameters were tested. In case of duplicated measurements, a mean value of resistivity has was taken. The array sequence 3D-CD included cross-line perpendicular and diagonal (with an angle above 60º against the parallel lines) nested array measurements taken with the current electrodes on the outer lines (Lines A and F) and the potential electrodes on the centre lines (Lines C and D). This could be referred to as quadruple-line offset configurations (Loke *et al.* 2014).

The array with the abbreviation 3D-DG was an array on four lines with a diagonal selection of electrodes, as the previous array configuration. The difference was in the angle of the quadrupole direction against the parallel lines that is smaller than 45º.

The array sequence 3D-GD was a variation of the multiple-gradient configuration using all the electrodes of the six lines as if they were in-line, however with one of the current electrodes on Line A and the other one on Line F, while the potential dipoles were spread along the remaining four lines. This could be referred to as multiple-line offset configurations (Loke *et al.* 2014).

The array named 3D-DD was an equatorial dipole–dipole configuration, where the current electrodes were chosen from two different lines and the potential electrodes are spread along the same lines; for example, the current dipole was represented by electrode number 1 of Lines C and D, whereas the potential dipoles were from electrodes 3 to 64 along the same lines. For this type of configuration, we used several line combinations; in particular, we measured using Lines A–F, B–E, C–D, A–E, B–F, A–C, B–D, C–E, A–D, C–F, and D–F.

The array named 3D-OT was designed to enhance the information orthogonal to the direction of the six parallel lines. It was essentially a Wenner–Schlumberger array using electrodes on four different lines; we utilised, for example, current electrode number 6 on Lines A and F and potential electrode number 6 along Lines C and D. Moreover, to make use of the six channels of the instrument (the maximum in this particular 3D configuration) and to increase the lateral resolution, we added adjacent potential dipoles at electrode numbers 1 to 11, again along Lines C and D. We repeated the same acquisition scheme moving the current electrodes to Lines B and E.

Data were acquired with an ABEM Terrameter LS using a 100% duty cycle with a minimum of two cycles and a constant length of pulses (2 seconds). The 100% duty cycle was chosen to effectively reduce the acquisition time. Chargeability data were obtained using the approaches of Olsson *et al.* (2015), where the on-time curve (charging effect) was translated in a decay curve and the standard calculation of apparent integral chargeability was calculated between 0.1 seconds and 2 seconds. With this approach, the charge and discharge effects were superimposed in the 100% duty cycle. Even though the current waveform in the

| Acronym | 2D array | 3D array | Description |
|---------|----------|----------|-------------|
| **2D-GD** | X | | Multiple gradient |
| **3D-CD** | | X | Cross-line diagonal and perpendicular |
| **3D-DG** | | X | Cross-line diagonal low angle |
| **3D-DD** | | X | Equatorial dipole–dipole |
| **3D-GD** | | X | Multiple gradient |
| **3D-OT** | | X | Orthogonal Wenner–Schlumberger |

**Table 1** Summary of the type of arrays acquired during the survey.
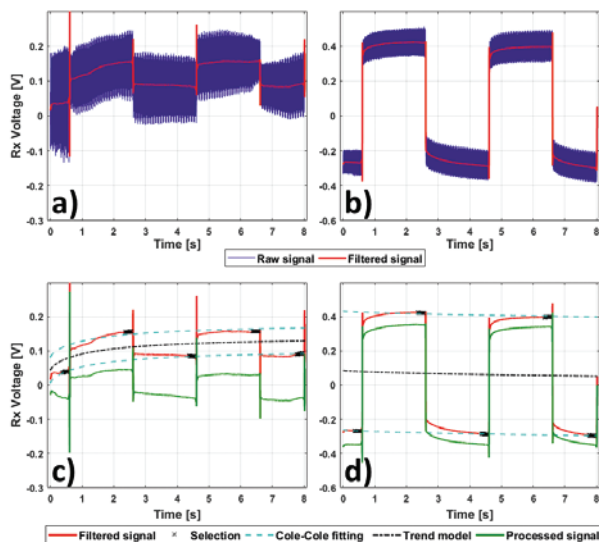
**Figure 3** Examples of processing of the potential full waveforms. Panels (a) and (b) show the raw data of two different full waveforms and the low-pass filter on every single pulse, while the ramp of the changing polarity is ignored. Panels (c) and (d) show the removing of the background drift, applied on the same full waveforms in (a) and (b), respectively.

present case was not modelled, as in Olsson *et al.* (2015), we believe that the estimated integral chargeability can give a good approximation and that it can be sufficient for a qualitative evaluation of the results. The full waveforms of potential dipoles were recorded with a sampling rate of 3.75 kHz.

Data were as far as possible collected during night, to avoid and/or reduce the persistent urban noise, as it was found beneficial in a prior test survey; nevertheless, many data points had a bad signal-to-noise ratio (SNR). The main sources of noise were due to (i) electrical powerlines (50 Hz harmonics), (ii) commuter and long-distance trains (16.67 Hz), and (iii) metro trains (DC current). The first two sources of noise were coherent and could easily be filtered out from the recorded waveforms. The disturbances from grounding points of the metro line were caused by DC current that added to the generated signal and that was highly complicated to handle and remove from the recorded signal.

In order to retrieve useful data, a number of processing steps were applied to the full-waveform data. An example of the processing on two different full waveforms is presented in Figure 3, where Figures 3(a) and (c) show the same dataset in two subsequent processing steps, as well as for Figures 3(b) and (c). The first processing stage consists of removing the harmonic noise and possible high-frequency spikes. The denoising procedure uses a low-pass filter to cancel the frequency content above 16.6 Hz. Care is needed in applying filters on DCIP full waveforms, since there are many issues in filtering a Heaviside step function; for example, the portions of the curve that are close to the "step" (change of current polarity) can be corrupted, and several filtering algorithms can lead to a phase shift of the on-time pulse. For these reasons,
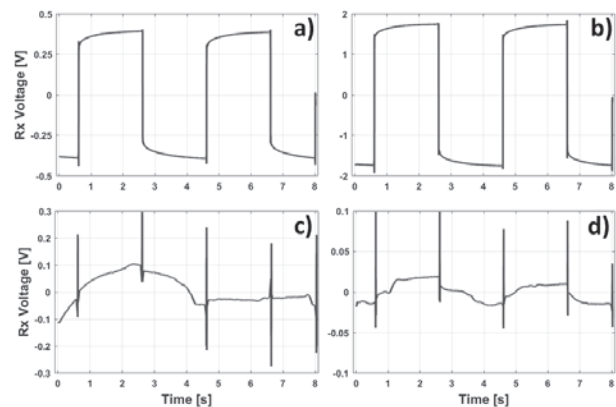


**Figure 4** Examples of processed full waveforms. Panels (a) and (b) show good quality of full waveforms, whereas panels (c) and (d) are affected by a high level of noise.

we have applied the Savitzky–Golay filter algorithm (Savitzky and Golay 1964) on every single pulse (see examples in Figures 3(a) and (b)), using a first-order polynomial and a frame length according to the wavelength of the signal that should be removed. Using these parameters, the filter acts as an averaging window, but it is better at preserving the portions of the curve that are adjacent to the "step". The filter is applied only on the pulses, excluding the data points where the current is changing polarity, often affected by spikes of electromagnetic induction effects.

The second processing stage is the removal of the background drift (Figure 3(c) and (d)). Ground self-potentials and polarisation of the electrodes (Dahlin 2000) can superimpose a background trend at the potential response derived from the injected current waveform. The filtering procedure consists of subtracting a Cole–Cole model fitted simultaneously on the positive and negative pulses, where the curve gets close to the asymptotic voltage (Olsson *et al.* 2016).

An example of processed full waveforms is plotted in Figure 4. It is evident that the filtered signal improves the quality of the waveforms to estimate reliable electrical resistance and induced polarisation responses (see cases in Figures 4(a) and (b)). Nevertheless, some of the waveforms are corrupted by the presence of a non-systematic noise (Figures 4(c) and (d)) and characterised by a shape of the curve that does not have any information derived by the controlled current injection. The source of the non-harmonic noise is the grounding spots of the metro line: a secondary injection of DC current that we cannot control and we do not know where it is exactly located. The nature of this coherent noise, which is independent of the instrumentation, is confirmed by the presence of the same pattern, superimposed on the voltage waveforms, in several simultaneous recording of potential dipoles, i.e., the different input channels of the instrument.

An automatic quality check of the monotonically increasing curve shapes is applied via the reduced chi-squared ($\chi^2$) statistical operator, i.e.,

$$\chi^2 = \frac{1}{(n-m)} \sum_{i=1}^{n} \frac{(X_i - M_i)^2}{\sigma_{X_i}^2} \ , \tag{1}$$

where $n$ is the number of observations, $X_i$ is the $i$-th observation $\sigma_{Xi}$, is the variance of the $i$-th observation, $M_i$ is the predicted model at the $i$-th observation, and $m$ is the number of model parameters.

Different types of model curves were tested to fit the data: second-order polynomial, exponential Debye, stretched-exponential Kohlrausch, and exponential Cole–Cole (for a review on these models, see Kohlrausch 1854; Hilfer 2002). The model used in the present work is the stretched-exponential Kohlrausch model, i.e.,

$$M_i = a e^{-(t_i/\beta)^\gamma + \delta} \ , \tag{2}$$

where $t_i$ is the $i$-th observation time and $\alpha$, $\beta$, $\gamma$, and $\delta$ are the model parameters to be inverted.

The assumption of the Kohlrausch model is arbitrary; any other model could be applied. Nevertheless, we have the necessity of a reference model to fit the data and a threshold to neglect measurements. Both the Kohlrausch and the Cole–Cole models showed low and comparable overall residuals after the nonlinear least square fitting, when tested on several observed potential pulses. The model applied to the entire dataset is the Kohlrausch

model, since the fitting is computationally less demanding than the Cole–Cole model.

The curve fitting and $\chi^2$ are calculated independently for every single pulse of the potential waveform (Figure 5), where the pulse length is coherent with the acquisition parameters. Due to instrumental settings, the first and last pulses are shorter (Figure 4(a)); therefore, they are not used in the estimation of electrical resistivity and integral chargeability. The observed potential curve is normalised with the maximum value of the pulse, and a common value of $\sigma_{X_i}^2$ is set at 3%. The variance is fixed with a trial-and-error procedure, visually checking the goodness of the fitted curves and analysing the residuals. The assumption of the Kohlrausch model in the algorithm adds *a priori* information about the shape of the curve that can be considered acceptable from a signal quality point of view. This decision can lead to an over-cleaning of the data, discarding also measures that show a low SNR but have a different charging feature. Nevertheless, a model should be applied in order to be able to remove bad data in a statistical framework.

All the pulses with $\chi^2 < 1$ are saved, and the values of resistivity and integral chargeability are estimated, if at least two pulses of the dipole measurement passed the goodness-of-fit test. The resistivity and integral chargeability for every potential dipole are calculated, averaging the pulses that passed the statistical test, with the possibility of estimating also the variance inside the measurement. This framework optimises the use of the full waveforms, since each pulse is individually processed. It may
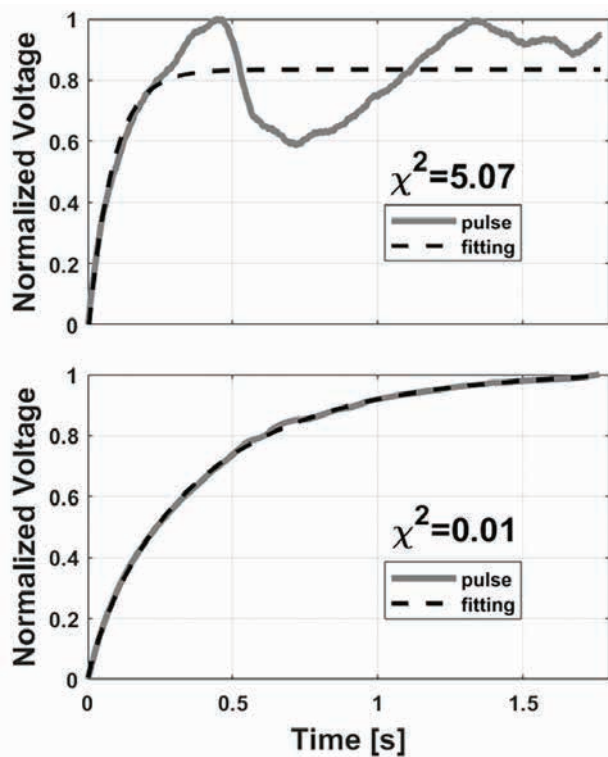


**Figure 5** Examples of quality check on the pulse shape with the goodness-of-fit test. The solid grey line is the processed full-waveform curve; the black dashed line is the stretched-exponential model.
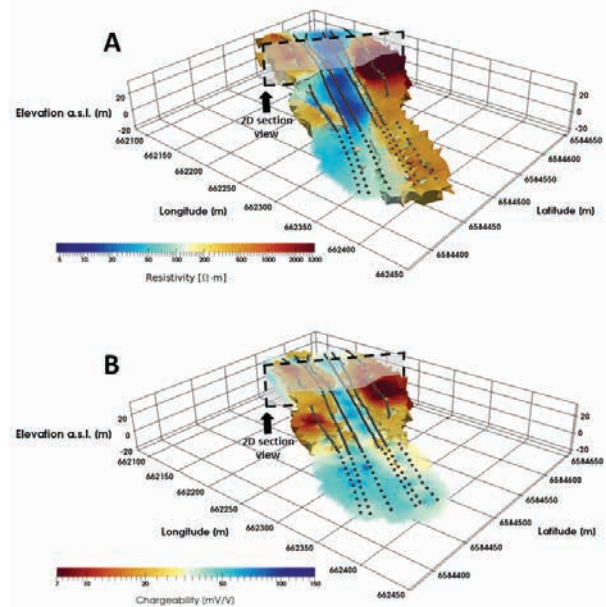


**Figure 6** Inverted 3D model of (A) electrical resistivity and (B) integral chargeability. The surface electrical values are plotted, with a shading of the low resistivity and high chargeability values. Black dots mark the electrode positions. The 2D vertical section plane in Figure 9 is shown together with the point of view. Coordinate system Sweref 99 TM.

happen that part of the potential waveform is represented by a high SNR, while the remaining portion is corrupted by the current grounding of the metro line. In these cases, we can keep only the portion of the waveform that shows a satsifactory goodness of the fit, avoiding to reject the entire dipole measurement.

The electrical resistance is calculated using the potential
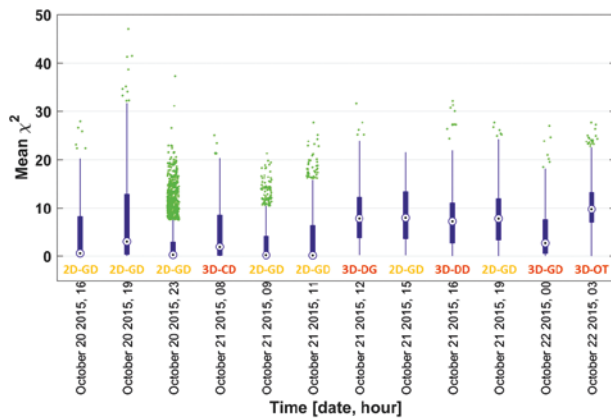


**Figure 7** The box plot shows the distribution of the mean values of the $\chi^2$ (reduced chi-square) for each measured quadrupole, grouped into acquired datasets. The thick blue line shows the values inside the 25th percentiles with a white circle for the median; the thin blue line represents the edges of the 75th percentiles; the green dots are outliers. The orange text defines the type of array for each dataset: the first two letters determine if the acquisition is two-dimensional (in-line, 2D) or three-dimensional (3D); the latter two letters after the dash indicate the type of array (see the Methodology section and Table 1).

value averaged on the last 0.3 seconds of the pulse before the changing of the current polarity.

The final cleaned dataset consists of about a third of the acquired data points (4,374 measurements), after the processing framework and the removal of the recordings with the maximum potential value less than 1 mV.

Figure 7 shows the distribution of the mean $\chi^2$ values, averaged over the number of pulses for each measurement. The datasets are grouped by the type of array and the acquisition date-time (mean value as the acquisitions can take several hours). It is not straightforward to define a trend in the quality distribution of the measurements, as it depends on several factors, i.e., the type of array and time of the day (the noise level is directly correlated to train traffic and human activity). In general, the quality is higher in the 2D acquisitions and in the 3D surveys where the overall geometric factor of the type of array is relatively small.. The dataset 3D-OT shows the higher geometrical factors, as well as some quadrupoles of 3D-DD. Measurements acquired during the day of 21st October are more affected by noise, and the 2D surveys show a distribution of the mean $\chi^2$ that is shifted towards higher values.

## RESULTS AND DISCUSSION

The processed and cleaned dataset was inverted using the 3D code BERT (Günther, Rücker and Spitzer 2006) for resistivity and, subsequently, for chargeability using pyGIMLi (Rücker, Günther and Wagner 2017). We used a tetrahedral mesh to incorporate the significant topography in the 50-m-deep model, using the measured electrode positions and additional points to constrain the topography outside of the ERT lines. The model crea-

**Table 2** Geotechnical probing positions with relative lithology and bedrock depth.

| Probing name | Coordinates | | | Depth interface between lithologies (m a.s.l.) | | |
| --- | --- | --- | --- | --- | --- | --- |
| | Sweref 99 TM (m) | | | Anthropogenic / Clay | Clay / Till | Till / Bedrock |
| | Y | X | elevation a.s.l. | | | |
| 12A526 | 6584569.38 | 662224.14 | 24 | 22.8 | 21.6 | 19 |
| 12A528 | 6584563.53 | 662196.58 | 23.8 | 23 | 16 | 13.2 |
| 12A530 | 6584567.77 | 662170.87 | 23.7 | 23.2 | 21.2 | 21.1 |
| 12A522 | 6584552.91 | 662220.78 | 23.7 | 22.6 | 16.4 | 14.6 |
| 12A524 | 6584550.55 | 662201.77 | 23.7 | 22.7 | 15.7 | 13.2 |
| 12A534 | 6584497.26 | 662287.45 | 23.4 | 22.7 | 19.2 | 18.8 |
| 12A532 | 6584561.24 | 662190.18 | 23.7 | 22.8 | 16 | 15.9 |
| 12A533 | 6584562.48 | 662208.94 | 23.7 | 22.7 | 15.5 | 13.1 |
| 12A521 | 6584554.14 | 662232.44 | 23.9 | 22.8 | 19.6 | 15.7 |
| 12A523 | 6584553.08 | 662211.27 | 23.8 | 22.7 | 15.3 | 13.6 |
| 12A525 | 6584553.20 | 662191.74 | 23.5 | 23.1 | 18.2 | 17.6 |
| 12A529 | 6584568.72 | 662185.14 | 23.8 | 22.9 | 17.7 | 16.6 |
| 12A527 | 6584569.38 | 662213.03 | 23.8 | 23.2 | 18.3 | 18.1 |
| 12A531 | 6584607.92 | 662133.32 | 23.5 | 22.7 | 19.3 | 19.2 |
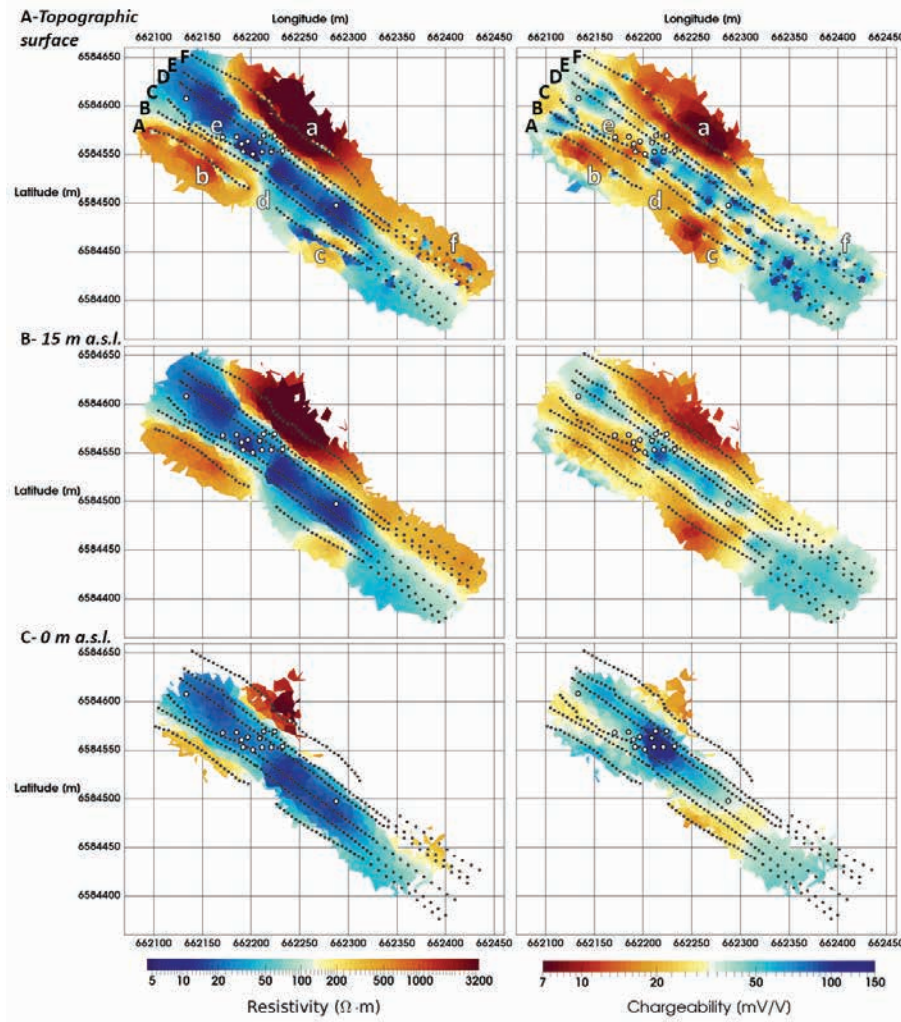
**Figure 8** Inverted 3D model of electrical resistivity and integral chargeability plotted as 2D horizontal slices at (A) topographic surface, (B) 15 m a.s.l., and (C) 0 m a.s.l. Black dots are the electrode positions, and the black circles (white filled) show the position of geotechnical drillings; they are projected on the horizontal slices. Black uppercased labels mark the location of the six parallel lines (Figure 1). White lowercased labels highlight the presence of features that are discussed in the Results and Discussion section. Coordinate system Sweref 99 TM.

tion follows the scheme of Udphuay *et al.* (2011) and uses several runs of the mesh generator to create a high-quality mesh with edge lengths of 5 m in the vicinity of the ERT lines and 30 m at the boundary. For the error model, we used a relative error of 5% and a voltage error of 1 mV, and discarded data with excessive errors completely. Additionally, a robust (L1 norm) data weighting was done to mitigate the influence of outliers. Likewise, an L1 model norm was used to resolve the high contrast between the resistive bedrock and the conductive sedimentary deposits. A value of 10000 Ωm was used as the upper resistivity limit using a logarithmic transform (using 0 as the lower limit). The regularization was a smoothness constraint of first order as explained in Günther *et al.* (2006) for irregular grids, using isotropic weights for all directions.

For inversion of the time-domain IP data after DC inversion, we implemented a new inversion scheme in the pyGIMLi framework that uses apparent chargeability as data points and chargeability as a model parameter, so that the target parameter is constrained directly using a model transform with 0 and 1 as lower and upper bounds, respectively. The forward problem involves,

going back to the formulation after Seigel (1959), another DC calculation with the model reduced by chargeability, and the Jacobian involves the DC Jacobian for the resistivity altered by the chargeability. As for the error model, we used 1 ms.

The inversion converged both for electrical resistivity and integral chargeability, obtaining a mean residual of the weighted squared error <1 in 15 iterations. The coverage, which is the overall integral sensitivity for all measurements in each model cell normalised by the cell volume, is a robust estimate of model resolution and, thus, reliability, as demonstrated by Ronczka *et al.* (2017). Therefore, we restricted all images of the results to a minimum threshold so that only well-resolved structures in the model are shown.

The inverted electrical resistivity values vary in a broad range: from the highly resistive rock mass (above 2000 Ωm), which coincides with the hummocky outcrop (Figures 1 and 2), to the conductive quaternary deposits (below 50 Ωm) in the middle of the investigated volume, mainly elongated around the road. The low-resistivity areas in the shallower ground coincide very well with the post-glacial clay and till deposits in Figure 2. Water
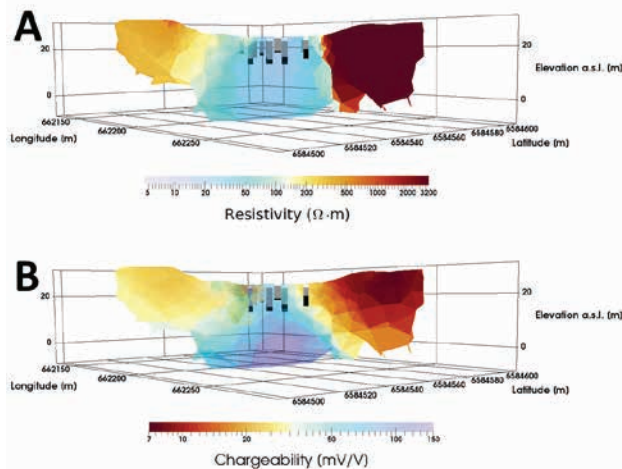
**Figure 9.** Inverted 3D model of (A) electrical resistivity and (B) integral chargeability, plotted as a 2D vertical section (see Figure 6 for the location of the plane). The geotechnical drillings are plotted as cylinders and are projected on the 2D plane: white colour is the top anthropogenic deposit, grey are the quaternary sediments, and black is granitoid rock. Coordinate system Sweref 99 TM.

sampled from a borehole (geotechnical probing 12A528, see Table 2), located in the median strip of the road, showed an anomalous high content of chloride anions (200 mg/l) and a Cl/Na ratio of 1.6 (Charlotte Sparrenbom, personal communication, November 2016). The percolating water around the road can be characterised by high conductivity, due to the de-icing agents that are spread during the winter season. This aspect can contribute to lowering the resistivity together with the presence of finer materials. The inverted integral chargeability has a trend similar to but opposite of resistivity. The rock outcrops are essentially non-polarisable, whereas the sedimentary deposits are slightly chargeable, mostly around 50 mV/V.

On the topographic surface of the inverted model (Figure 8(A)), stripes of contrasting electrical properties are aligned beside the electrode lines, e.g., along Line F (northern line, feature "a") on the resistive bedrock outcrop. This detail can be explained by the fact that we placed the electrodes alongside a small depressed lineament of the rock mass, where some soil could retain moisture and reduce the contact resistance. Similar linear features are present on Line A (southern line, features "b" and "c"). In particular, in the central part of the line (feature "c"), a conductive strip is cutting a more resistive body. This result can be explained by the diverse spatial resolution of the acquisition, where a shorter electrode spacing in-line allows detailed information on the shallower soil, whereas the distance between cross-line electrodes (Lines A and B) leads to an integration of larger and deeper volumes. This is the same cause that explains why an extremely conductive area is present where the road is built, instead of a shallow resistive anthropogenic layer.

The chargeability values at the surface (Figure 8(A)) show some behaviors that seem related with the electrode positions.

These irregularities can be due to the presence of fences and pipelines in the shallower portion of the subsoil. The processed raw data show a coherent signal, but it can be the result of non-geological man-made materials. For example, there were parts of a fence, close to Lines C and E, and manholes in the southern part of the area. These features disappear in the deeper portion of the investigated volume (Figure 8, forms B and C).

The distribution of electrical properties in the investigated volume shows two main classes of material: one is low resistive and chargeable sediments and weathered/fractured rock, and the other is highly resistive and non-polarisable fresh rock. In any case, there are some features that show a different trend in the distributions of electrical properties. The areas marked by the letters "d" and "e" in Figure 8(A) show low electrical resistivity (max. 100 Ωm) and low chargeability (around 20 mV/V). In the area of the low-resistivity anomaly "d", there is a man-made embankment for the metro line and a pillar below the bridge (see Figure 1). The presence of an area with a heavy anthropogenic reworking can explain this anomaly. Inside and around area "e", there are geotechnical probings, but the drilling logs do not show any significant variability in the geological materials. Actually, we do not have any explanation for the lower integral chargeability values. The outcrop in the southeastern part (feature "f") is characterised by relatively high resistivity, around 500 Ωm, and medium inverted chargeability, from 20 to 50 mV/V. The topographic elevation along Line F drops in the SE direction, from the most elevated point around area "a" to area "f". Similarly, the resistivity values are decreasing in the same direction, whereas the integral chargeability is decreasing. This aspect can be due to the quality of the rock mass, which may be higher in the most elevated part (so less eroded) and lowering down towards the depression with a sedimentary cover, where different systems of fractures are intersecting (see Figure 2).

Several geotechnical drillings are located around the road (Figures 8(A) and 9). All the 14 dynamic probings were drilled a few metres into the bedrock (usually about 3 m) with the recovery of disturbed samples (Table 2). The mean depth of the bedrock surface is about 16 m a.s.l. (around 8 m from ground level), with a wide range of variability considering the small distance between the probings, from a minimum of 13 m to a maximum of 21 m a.s.l. The interpolated bedrock surface looks very hummocky, with mounds and depressions.

In Figure 9, a direct comparison between the inverted electrical properties and the geotechnical information shows a huge discrepancy in the interpretation of the bedrock structures. The geophysical quantities alongside the hypothetical fracture zone (Figure 2) are similar to the quantities of the sedimentary cover. Both resistivity and chargeability distributions suggest the occurrence of a weak zone in the rock mass. According to geophysical data, the zone that can be interpreted as poor-quality bedrock is a sub-vertical feature with a NW–SE direction, about 40 m wide and elongated in the entire explored ground volume. The shape of the assumed fractured region is coherent

with the supposed delineation of the "heavily fractured zone" in Figure 2.

High electrical conductivity associated with the bedrock in this geological setting can only be justified by the presence of discontinuities with a high water content and probably filled by sedimentary fine material or products from a pervasive alteration of the granitoid rock into clay minerals. This aspect can also describe the relatively larger polarisation effect, in comparison with the adjacent fresh rock. It should be noticed that the sensitivity in the shallow volume (from ground surface down to 0 m a.s.l.) is high enough to be able to resolve the real distribution of the electrical properties with low uncertainty.

The incongruity with the geotechnical drillings could be explained by the nature of the weak zone itself: the crushed rock consist of boulders or large portions of fresh rock, interrupted by discontinuities and pervasive fractures (Morfeldt 1993). The geotechnical probing stops when it encounters 1–3 m of relatively compact rock, but few metres away a clay weathered fracture can be present. This can also explain the rugged bedrock topography, non-compatible with the geological evolution of the glacial landscape.

A proof of the deep expansion of the weak zone can be found in Roslin, Veseley and Salmonson (2018), where a detailed description of the evolution of the bypass passage design is reported. The rock quality was predicted by the geotechnical survey as very good, with a rock mass quality value (Q) higher than 10 (Barton et al. 1974). Several core drillings, intended to verify a later jet-grouting operation with the aim to stabilise and reduce the hydraulic permeability of the shallower sedimentary cover, revealed an unexpected poor rock quality with a Q value below 0.1. Taking into account this aspect, the jet-grouting volume had to be enlarged, and part of the construction design had to be updated.

As illustrated in the present case, the information achieved by the geophysical survey can complement and integrate the *in situ* geotechnical measurements, leading to a more comprehensive engineering geological model with less uncertainty, to be used for the design and planning of the underground infrastructure. Also, further geotechnical investigations might be suggested based on the results from the geophysics.

## CONCLUSIONS

Geophysical measurements in urban environments can be very complicated to carry out due to the restrictions of available space and the high noise levels. One way to deal with noise is careful processing of the recorded waveforms. A deeper understanding of raw data can lead to a more accurate use of the measured quantities, improving the reliability of electrical resistivity and IP estimations.

Geophysical techniques can be effective in complementing traditional geotechnical sounding, as they produce continuous 2D/3D images of subsoil properties. In particular, geoelectrical methods investigate underground properties that are linked to water saturation, mineral alteration, and fine sediment content.

These quantities are not straightforwardly estimated by localized geotechnical probing, which is essential for calibrating and interpreting the geophysical results, since it can miss the actual distribution of subsoil structures. In the present case, the geotechnical probing did not identify the real geometry of the weak zone, which was extending deeper than expected. Furthermore, the weak zone in the bedrock had not been identified in the site investigation. Only a second campaign of drilling, for testing a jet-grouting operation, revealed the poor quality of the rock mass. The DCIP survey carried out in the suburban environment of Stockholm, even though restricted by logistical constraints, shows a 3D model of a large volume of the underground. The inverted geophysical quantities suggest the presence of an interpreted wide fracture zone, later confirmed by the construction work, which can potentially cause severe problems in the realisation of underground infrastructure.

## REFERENCES
Barton N., Lien R. and Lunde J. 1974. Engineering classification of rock masses for the design of tunnel support. *Rock Mechanics* **6**(4), 183–236.
Bell F.G. 2006. *Engineering Geology*, 2nd edn. Elsevier, 592pp.
Bellmunt F., Marcuello A., Ledo J., Queralt P., Falgàs E., Benjumea B. et al. 2012. Time-lapse cross-hole electrical resistivity tomography monitoring effects of an urban tunnel. *Journal of Applied Geophysics* **87**, 60–70.
Cardarelli E., Cercato M., Cerreto A. and Di Filippo G. 2010. Electrical resistivity and seismic refraction tomography to detect buried cavities. *Geophysical Prospecting* **58**, 685–695.
Cavinato G.P., Di Luzio E., Moscatelli M., Vallone R., Averardi M., Valente A. et al. 2006. The new Col di Tenda tunnel between Italy and France: integrated geological investigations and geophysical prospec-

tions for preliminary studies on the Italian side. *Engineering Geology* **88**(1–2), 90–109.

Dahlin T. 2000. Short note on electrode charge-up effects in DC resistivity data acquisition using multi-electrode arrays. *Geophysical Prospecting* **48**, 181–187.

Dahlin T. and Zhou B. 2006. Multiple-gradient array measurements for multichannel 2D resistivity imaging. *Near Surface Geophysics*, **4**, 113-123.

Danielsen, B.E. and Dahlin, T., 2009. Comparison of geoelectrical imaging and tunnel documentation. *Engineering Geology* **107**, 118–129.

Ganerød G.V., Rønning J.S., Dalsegg E., Elvebakk H., Holmøy K.H., Nilsen B. *et al.* 2006. Comparison of geophysical methods for subsurface mapping of faults and fracture zones in a section of the Viggja road tunnel, Norway. *Bulletin of Engineering Geology and the Environment* **65**, 231–243.

Geoarkivet 2017. *Stockholms stad, Geoarkivet. www.stockholm.se/geoarkivet*. Last access: September 2017.

Günther T., Rücker C. and Spitzer K. 2006. Three-dimensional modelling and inversion of DC resistivity data incorporating topography—Part II: Inversion. *Geophysical Journal International* **166**, 506–517.

Hilfer R. 2002. Analytical representations for relaxation function of glasses. *Journal of Non-Crystalline Solids* **305**, 122–126.

Kohlrausch R. 1854. Theorie des elektrischen Rückstandes in der Leidner Flasche. *Annalen der Physik und Chemie* **91**, 56–82, 179–213.

Lantmäteriet**.** 2016. GSD-Ortophoto 1m raster resolution. *https://www. lantmateriet.se/*. Last access: December 2016.

Loke M.H., Wilkinson P.B., Uhlemann S.S., Chambers J.E. and Oxby L.S. 2014. Computation of optimized arrays for 3-D electrical imaging surveys. *Geophysical Journal International* **199**(3), 1751–1764.

Malehmir A., Zhang F., Dehghannejad M., Lundberg E., Döse C., Friberg O. *et al.* 2015. Planning of urban underground infrastructure using a broadband seismic landstreamer—Tomography results and uncertainty quantifications from a case study in southwestern Sweden. *Geophysics* **80**, B177–B192.

Morfeldt C.O. 1993. Underground construction on engineering geological terms: a fundamental necessity for the function of metropolitan environments and Man's survival. *Engineering Geology* **35**, 149–165.

Olsson P.-I., Dahlin T., Fiandaca G. and Auken E. 2015. Measuring time domain spectral induced polarization in the on-time—Decreasing the acquisition time and increasing the signal levels. *Journal of Applied Geophysics* **123**, 316–321.

Olsson P.-I., Fiandaca G., Juul Larsen J., Dahlin T. and Auken E. 2016. Doubling the spectrum of time-domain induced polarization by harmonic de-noising, drift correction, spike removal, tapered gating and data uncertainty estimation. *Geophysical Journal International* **207**, 774–784.

Papadopoulos N., Sarris A., Yi M.J. and Kim J.K. 2009. Urban archaeological investigations using surface 3D Ground Penetrating Radar and Electrical Resistivity Tomography methods. *Exploration Geophysics* **40**, 56–68.

Perrone A., Zeni G., Piscitelli S., Pepe A., Loperte A., Lapenna V. *et al.* 2006. Joint analysis of SAR interferometry and electrical resistivity tomography surveys for investigating ground deformation: the case-study of Satriano di Lucania (Potenza, Italy). *Engineering Geology* **88**, 260–273.

Perrone A., Vassallo R., Lapenna V. and Di Maio C. 2008. Pore water pressures and slope stability: a joint geophysical and geotechnical analysis. *Journal of Geophysics and Engineering* **5**, 323–337.

Rücker C., Günther T. and Wagner F.M. 2017. pyGIMLi: an open-source library for modelling and inversion in geophysics. *Computers & Geosciences* **109**, 106–123.

Persson L. 1998. Engineering geology of Stockholm, Sweden. *Bulletin of Engineering Geology and the Environment* **57**, 79–90.

Ronczka M., Hellman K., Günther T., Wisen R. and Dahlin T. 2017. Electric resistivity and seismic refraction tomography, a challenging joint underwater survey at Aspö hard rock laboratory. *Solid Earth* **8**, 671–682.

Roslin M., Vesely J. and Salmonson P. 2018. Passage under Lövstavägen at Bypass Stockholm—From design to realization. *Proceedings of Bergdagarna (20-21 mars 2018). http://www.befoonline.org/ UserFiles/Dokument/Bergdagarna_2018/Artiklar_2018/BM_5.pdf*. Last access: March 26, 2018.

Rønning J.S., Ganerød G.V., Dalsegg E. and Reiser F. 2014. Resistivity mapping as a tool for identification and characterisation of weakness zones in crystalline bedrock: definition and testing of an interpretational model. *Bulletin of Engineering Geology and the Environment* **73**, 1225–1244.

Savitzky A. and Golay M.J.E. 1964. Smoothing and differentiation of data by simplified least squares procedures. *Analytical Chemistry* **36**, 1627–1639.

Seigel H. 1959. Mathematical formulation and type curves for induced polarization. *Geophysics* **24**, 547–563.

Stålhös G. 1968. Map of solid rocks of the Stockholm region. *Geological Survey of Sweden* Ba **24**.

Stålhös G. 1969. Description to the map of solid rocks Stockholm (*in Swedish*). *Geological Survey of Sweden* Ba **24**, 1–190.

Tsokas G.N., Tsourlos P.I., Vargemezis G. and Novack M. 2008. Non-destructive electrical resistivity tomography for indoor investigation: the case of Kapnikarea Church in Athens. *Archaeological Prospection* **15**, 47–61.

Udphuay S., Günther T., Everett M.E., Warden R.R. and Briaud J.-L. 2011. Three-dimensional resistivity tomography in extreme coastal terrain amidst dense cultural signals: application to cliff stability assessment at the historic D-Day site. *Geophysical Journal International* **185**, 201–220.